Electron paramagnetic resonance and optical spectroscopy of Ti-doped $CaYAlO_4$

1994 J. Phys.: Condens. Matter 6 4381

(http://iopscience.iop.org/0953-8984/6/23/018)

J. Phys.: Condens. Matter 6 (1994) 4381–4394. Printed in the UK

Electron paramagnetic resonance and optical spectroscopy of Ti-doped $CaYAlO_4$

M Yamaga†, T Yosida‡, Y Naitoh§ and N Kodama§

† Department of Physics, Faculty of General Education, Gifu University, Gifu 501-11, Japan
‡ Nakanihon Automotive College, Sakahogi, Kamo 505, Japan
§ Tosoh Corporation, Hayakawa, Ayase 252, Japan

Received 14 December 1993, in final form 16 March 1994

Abstract. Ti-doped $CaYAlO_4$ crystals were grown in a reducing atmosphere. The absorption spectrum with peaks at 408 nm and 540 nm observed at room temperature was strongly polarized along the a and b axes. EPR measurements in the temperature range of 4.2–300 K have found that Ti^{3+} ions in $CaYAlO_4$ show orthorhombic symmetry. In order to explain the optical and EPR results, we have proposed that the Ti^{3+} ions are perturbed by an O^{2-} ligand ion vacancy on the c axis and additionally by either an Al^{3+} ion vacancy or a substituted Ti^{4+} ion at neighbouring Al^{3+} ion sites in the c plane containing the Ti^{3+} ions. This model can explain the polarization of the absorption spectrum and, also, enable us to deduce that the absorption bands with peaks at 408 nm and 540 nm are due to the perturbed $Ti^{4+}$and Ti^{3+} octahedra, respectively.

1. Introduction

Transition metal ions (Ti^{3+}, Cr^{3+}, Cr^{4+}, Co^{2+} and Ni^{2+}) have been used as laser active ions in tunable solid state laser materials [1]. Ti^{3+}:sapphire is a promising tunable solid state laser material [2]. The tuning range is in the infrared region of 0.7–1.1 μm. Recently, Ti^{3+}-doped $YAlO_3$ has attracted considerable interest in view of its potential as a tunable solid state laser material operating at shorter wavelengths than Ti^{3+}-doped Al_2O_3. However, the laser action of Ti^{3+}:$YAlO_3$ has not been successful due to the excited state absorption [3, 4]. In order to achieve a laser action in blue and green regions, the development of Ti^{3+} host crystals is required.

The energy of light emitted from Ti^{3+} ions in crystals is determined by the crystal field splitting of Ti^{3+}, which is represented by [5]

$$10Dq = \frac{5Ze^2\langle r^4\rangle}{12\pi\varepsilon_0 a^5} \tag{1}$$

where $-Ze$ is the charge of a ligand ion, $\langle r^4\rangle$ is the average of r^4 for 3d orbitals and a is the distance between the central and ligand ions. Equation (1) indicates that the crystal field splitting increases with the decrease of the distance, a. The distances, a, for Al_2O_3 [6], $YAlO_3$ [7] and $CaYAlO_4$ [8] are summarized in table 1. The crystal field splitting of Ti^{3+} ions in $CaYAlO_4$ is expected to be larger than those in Al_2O_3 and $YAlO_3$, resulting in a blue shift of the Ti^{3+} luminescence [9]. This paper describes the crystal growth of Ti-doped $CaYAlO_4$ with K_2NiF_4 structure, the electron paramagnetic resonance (EPR), the absorption, the luminescence and the excitation spectra.

0953-8984/94/234381+14$19.50

Table 1. Distances between a central ion and ligand ions of an octahedron in oxide crystals.

Crystal	Distance (Å)
Al_2O_3	Al–O(I)=1.86
	Al–O(II)=1.97
$YAlO_3$	Al–O(I)=1.901
	Al–O(II)=1.911
	Al–O(III)=1.921
$CaYAlO_4$	Al–O(I)=1.784
	Al–O(II)=1.824

2. Crystal structure

Figure 1 shows the structure of $CaYAlO_4$ with space group $I4/mmm$ (D_{4h}^{17}) [8]. Ca^{2+} and Y^{3+} ions are distributed at random keeping the composition ratio of 1:1. The lattice constant $a = b = 3.648$ Å and $c = 11.89$ Å. An octahedron surrounding an Al^{3+} ion is slightly compressed along the c axis, where the distances between Al^{3+} and O^{2-} ions located along the a and c axes are 1.824 Å and 1.784 Å, respectively. Ti^{3+} and Ti^{4+} ions preferentially occupy Al^{3+} sites.

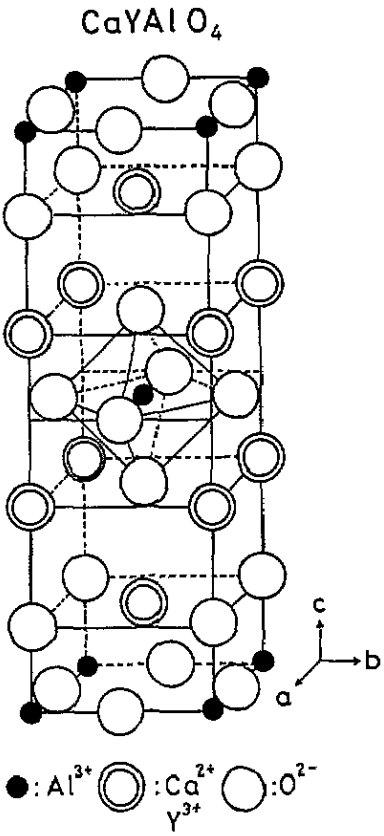

Figure 1. Crystal structure of $CaYAlO_4$.

3. Crystal growth and experimental procedure

Single crystals of Ti-doped $CaYAlO_4$ (CYA) were grown by the Czochralski technique from melts prepared in iridium crucibles with high-purity components $CaCO_3$(5N):Y_2O_3(5N):Al_2O_3(5N)=2:1:1. Up to 2 mol% TiO_2 (2.4×10^{20} cm^{-3}) were added to the powdered charges. The crystal growth was carried out in a reducing atmosphere (1% H_2:99% Ar) in order to convert Ti^{4+} to Ti^{3+}. The pulling rates and seed rotation rates were 0.8–3.0 mm h^{-1} and 5 rpm, respectively. The resulting boule was cut and polished into samples with approximate dimensions $4 \times 4 \times 4$ mm^3, the cut faces being normal to ⟨100⟩, ⟨010⟩ and ⟨001⟩ directions of the crystal. Some of these samples were studied by EPR and optical techniques (AS#H_2TI:CYA sample). Other samples from this boule were annealed in a reducing atmosphere (5% H_2:95% Ar) or an oxidizing atmosphere (air) at 1500 °C for 20 h. The former is denoted by ANN#H_2TI:CYA; the latter is denoted by ANN#O_2TI:CYA. Pure $CaYAlO_4$ crystals were, also, grown in an inert atmosphere (AS#CYA sample). Some samples from the boule were annealed in a reducing atmosphere (ANN#H_2CYA sample) and in an oxidizing atmosphere (ANN#O_2CYA sample), compared with Ti-doped $CaYAlO_4$ crystals.

EPR measurements were made at temperatures in the range 4.2–300 K using a Varian X-band EPR spectrometer employing 270 Hz field modulation. The polarization of the optical absorption spectrum was measured at room temperature by inserting a linear polarizer in a conventional double-beam spectrometer. The emission and the excitation spectra were measured using a Hitachi MPF4 fluorescence spectrometer at room temperature.

4. Experimental results

4.1. Optical measurements

The as grown pure $CaYAlO_4$ crystal (AS#CYA sample) is brown in colour. The absorption has a broad band with the peak at 420 nm, of which the coefficient is about 1 cm^{-1}, as shown in figure 2(a). The samples after the thermal treatment are transparent. The absorption spectrum for the ANN#H_2CYA sample is shown in figure 2(b). The Ti-doped $CaYAlO_4$ crystal (AS#H_2TI:CYA sample) shows strong absorption in the visible range. The absorption spectrum consists of two bands with peaks at 408 nm and 540 nm as shown in figure 3(a). These bands are completely polarized along the *a* and *b* axes ($E \parallel$ ⟨100⟩, ⟨010⟩). The absorption coefficients at 408 nm and 540 nm depend strongly on the condition of the crystal growth. They increase abruptly as the partial H_2 pressure increases (0.5% → 5%). Such large absorption coefficients are caused by the parity-allowed transition, that is, the transition is electric dipole in nature. Annealing the as grown sample in a reducing atmosphere (ANN#H_2TI:CYA sample) decreases somewhat the intensities of these absorption bands, whereas the two bands disappear completely for the ANN#O_2TI:CYA sample as shown in figure 3(b). The partial H_2 pressure in a crystal growth process may produce O^{2-} vacancies, whereas annealing the as grown sample in an oxidizing atmosphere may recover O^{2-} ions. Then, the 408 nm and 540 nm absorption bands may be associated with not only Ti ions, but also O^{2-} vacancies.

Luminescence excited in both bands could not be observed in the AS#H_2TI:CYA and ANN#H_2TI:CYA samples. This fact indicates that the centres corresponding to these bands deexcite non-radiatively to the ground state.

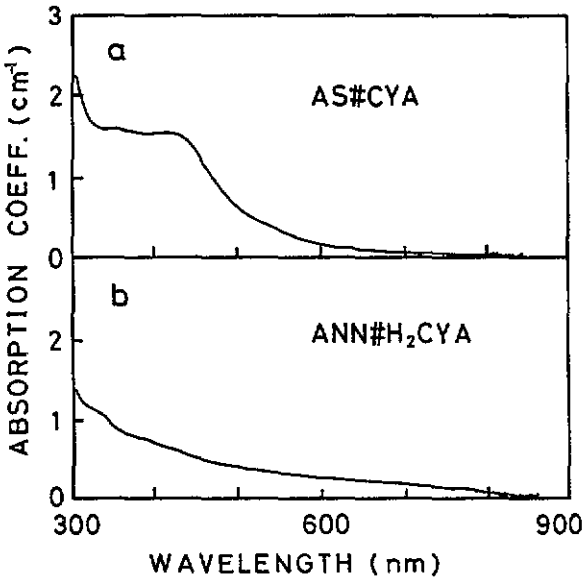

Figure 2. Absorption spectra of pure $CaYAlO_4$ crystals, (a)AS#CYA sample and (b) ANN#H_2CYA sample, observed at room temperature. Light propagates along the *c* axis of the crystal.

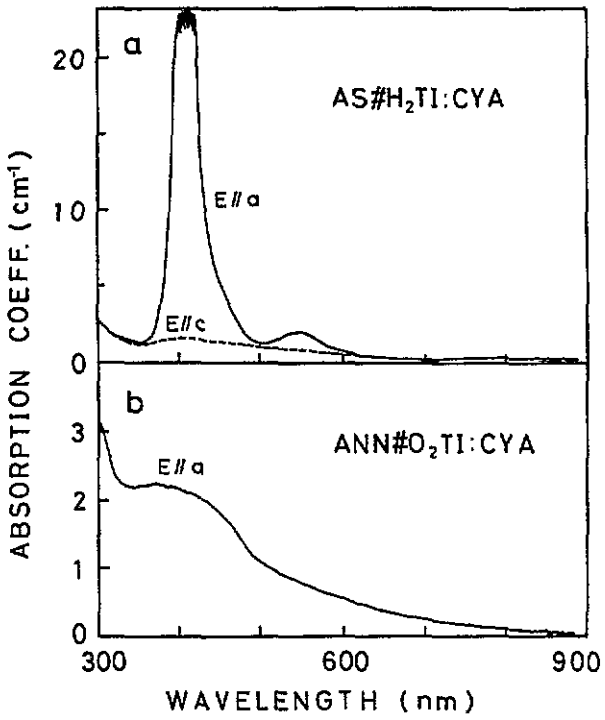

Figure 3. Absorption spectra of Ti-doped $CaYAlO_4$ crystals, (a) AS#H_2TI:CYA sample and (b) ANN#O_2TI:CYA sample, observed at room temperature.

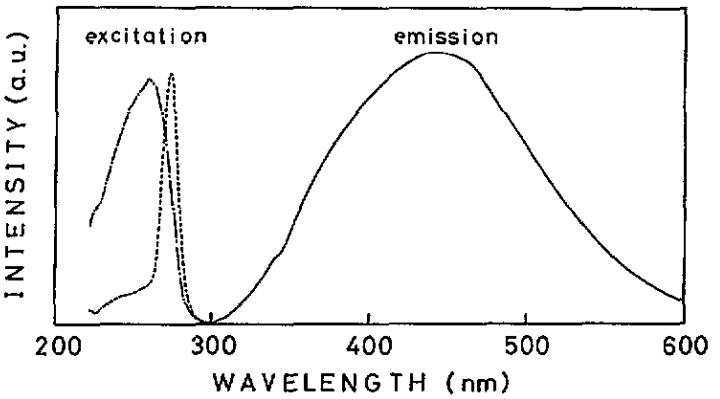

Figure 4. Emission and UV excitation spectra of Ti^{4+} in the AS#H_2TI:CYA sample observed at room temperature. The excitation spectra (- - - -) and (— - —) measure the intensities of the 465 nm broad band emitted from the bulk sample and from the UV irradiated surface, respectively. The spectra are normalized.

UV excitation at 275 nm for the AS#H_2TI:CYA sample produces a broad emission band with the peak at 465 nm as shown in figure 4. The excitation spectrum of the emission detected at the fixed wavelength of 465 nm comprises two bands with peaks at 260 nm and 275 nm. The radiation emitted under 260 nm excitation comes only from the surface; that emitted under 275 nm excitation comes from the bulk sample. The blue emission could not be observed in the AS#CYA sample. The emission and excitation spectra are very similar to those observed in Ti^{4+}:Al_2O_3 grown in an oxidizing atmosphere [10]. The UV excitation spectra below 300 nm are due to the charge transfer transition between Ti^{4+} and O^{2-} ions. Then, the radiative centre is assigned to be an isolated Ti^{4+} ion in $CaYAlO_4$.

4.2. EPR measurements

The sample preparation and the optical spectra demonstrate that the 408 nm and 540 nm absorption bands are associated with complexes of Ti ions and oxygen vacancies, but do not give structural information. The EPR technique provides detailed structural information on transition metal ions in insulating materials.

The EPR measurements were carried out for the AS#H_2TI:CYA sample. The EPR transitions were relatively easily saturated at low temperatures, even at low microwave power levels. Figure 5 shows the temperature dependence of EPR spectra measured at a microwave power of 0.01 mW and a microwave frequency of 9.486 GHz. The broad A line for $B \parallel \langle 001 \rangle$ (c axis) in figure 5(a) is shifted to lower magnetic field and decreases in intensity with the increase of temperature. The A line disappears above 93 K, whereas the new weak B and D lines appear above 47 K, being stable up to room temperature. The shift of the A line for $B \parallel \langle 110 \rangle$ in figure 5(b) is small compared with that for $B \parallel \langle 001 \rangle$. Figure 6 shows the temperature dependence of the resonance field positions for $B \parallel \langle 001 \rangle$ and $B \parallel \langle 110 \rangle$. The line width of the A line for $B \parallel \langle 001 \rangle$ and 16 K, being equal to the peak to peak distance of the first derivative, is about 80 G. It is much larger than that (15 G) observed in Ti^{3+}:$YAlO_3$ [11]. The inhomogeneous broadening of the A line observed at low temperatures may be produced by random distortion of Ca^{2+} and Y^{3+} in figure 1. Usually, Ti^{3+} EPR signals are broadened and undetectable by rapid spin–lattice relaxation with increasing temperature [11–14]. The large shift of the A line at $B \parallel \langle 001 \rangle$ and the

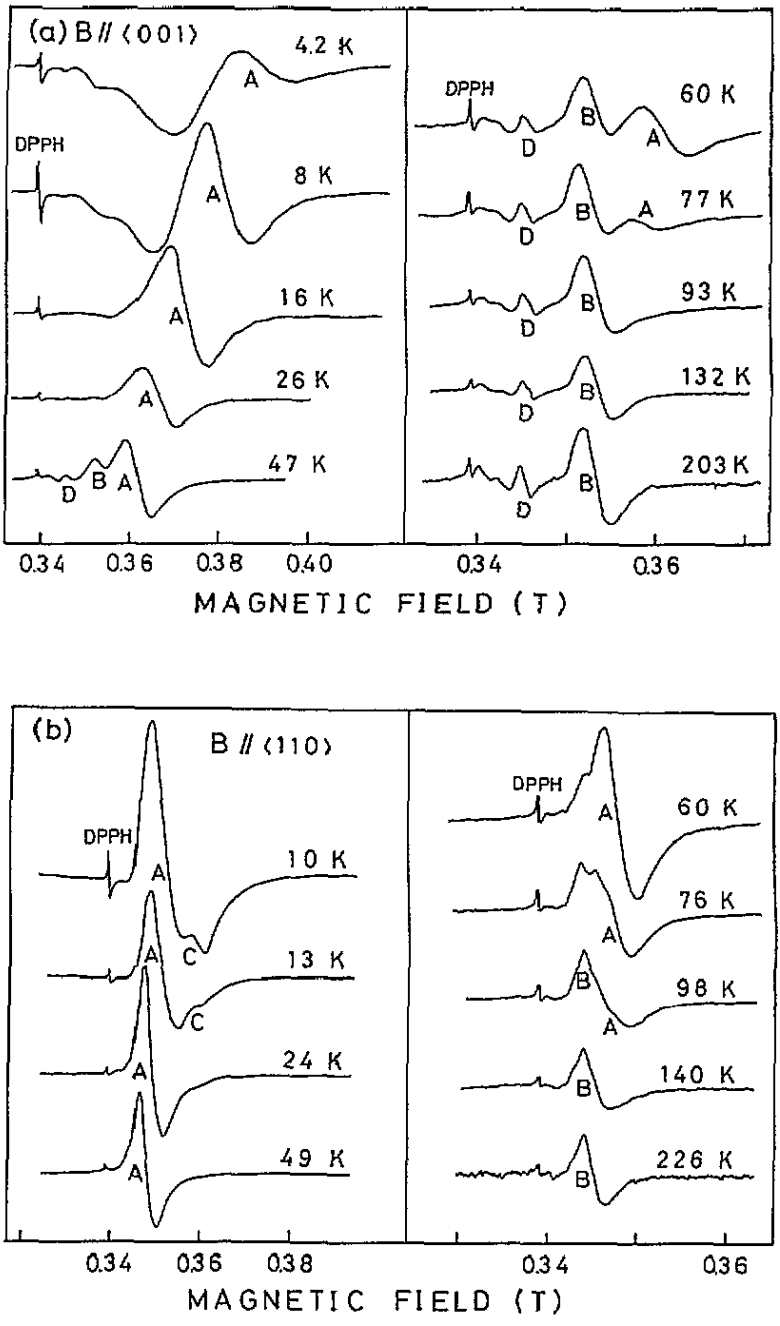

Figure 5. Temperature dependence of the EPR spectra of Ti^{3+} in the AS#H_2TI:CVA sample with magnetic fields applied (a) ‖ ⟨001⟩ and (b) ‖ ⟨110⟩.

decrease of the intensity with increasing temperature may be due to the combination of the

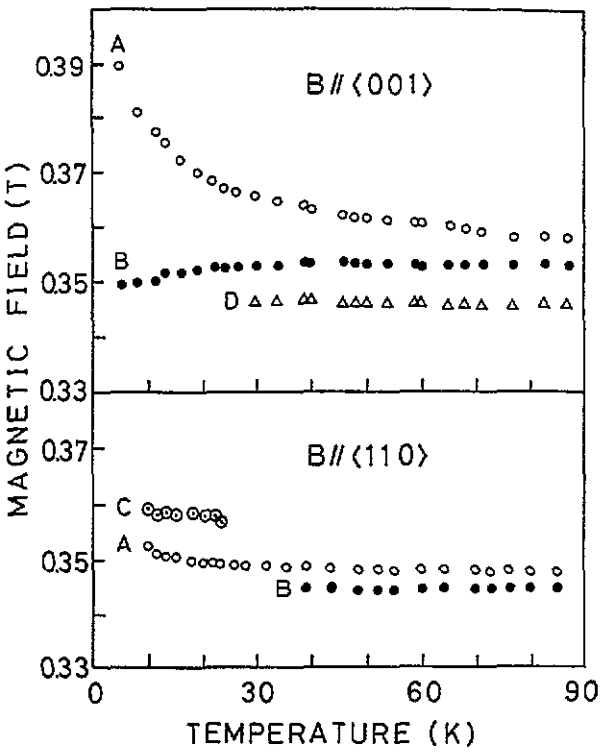

Figure 6. Temperature dependence of the resonance fields at $B \parallel \langle 001 \rangle$ and $B \parallel \langle 110 \rangle$.

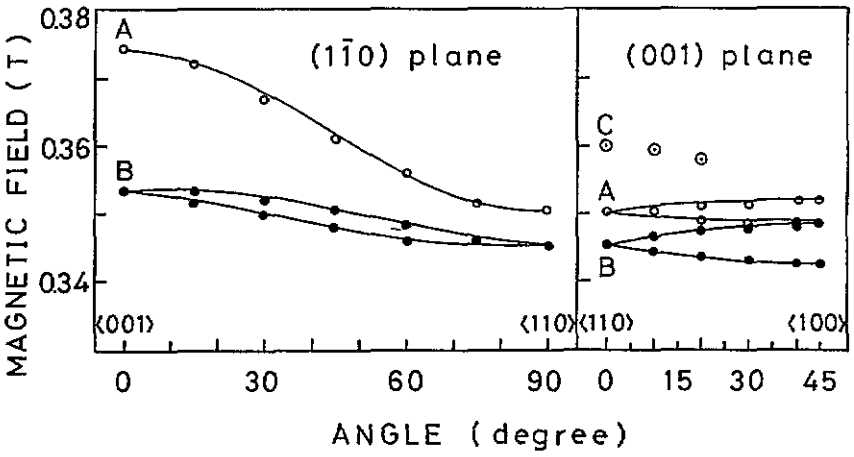

Figure 7. Angular variations of the EPR spectra of Ti^{3+} in the AS#H_2TI:CYA sample with the magnetic field in the (1$\bar{1}$0) and (001) planes. Solid curves for the A and B lines are calculated using (2) and the spin Hamiltonian parameters in table 2.

random and spin relaxation effects. A detailed discussion will be given in the next section.

Figure 7 shows the angular dependence of the EPR spectra as the magnetic field is rotated

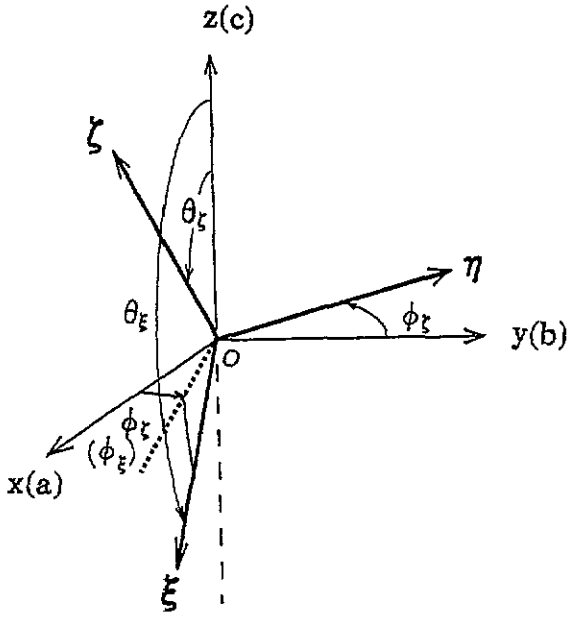

Figure 8. Definition of principal ξ, η, ζ axes and their polar angles for the Ti^{3+} ion with respect to the *abc* coordinate system.

in the (001) and (1$\bar{1}$0) planes. The circles in figure 7 represent the resonance field positions. The angular variations of the A line were observed at 20 K. The A line at any magnetic field direction in the (1$\bar{1}$0) plane is a single line, whereas the line splits into two branches for the magnetic field applied in the (001) plane. These results indicate that the three principal axes are parallel to the ⟨100⟩, ⟨010⟩ and ⟨001⟩ directions of the crystal and that the A line is due to two structually equivalent sites which become magnetically equivalent when the magnetic field is applied in the (1$\bar{1}$0) plane. The angular variations of the B line were observed at 230 K. The B line splits into two branches in the (1$\bar{1}$0) plane and collapses for $B \parallel \langle 001 \rangle$ and ⟨110⟩ directions. The directions with the maximum and minimum resonance fields are not parallel to the ⟨001⟩ and ⟨110⟩ directions, but shifted by 10° from them.

The angular dependences of the A and B lines are fitted by the spin Hamiltonian

$$\mathcal{H} = \mu_B(g_\xi S_\xi B_\xi + g_\eta S_\eta B_\eta + g_\zeta S_\zeta B_\zeta) \tag{2}$$

where S is $\frac{1}{2}$, and μ_B is the Bohr magneton. The principal axes ξ, η and ζ of the g tensor and the polar angles (θ_ξ,ϕ_ξ) for the ξ axis and $(\theta_\zeta,\phi_\zeta)$ for the ζ axis are defined in figure 8. The principal ζ axis is defined as the magnetic field direction with the maximum of the g value, being closest to that of the free electron ($g_e = 2.0023$). The solid curves in figure 7, calculated using (2) with the spin Hamiltonian parameters and the polar angles of the principal axes listed in table 2, fit the angular variations of the A and B lines. The principal ζ axis of the A line is parallel to the ⟨100⟩ or ⟨010⟩ axis, whereas that of the B line is bent by 10° towards the ⟨001⟩ direction from that of the A line. The C line is only observable near the ⟨110⟩ direction. Assuming that the observed branch is a higher-field component and the principal axis is parallel to the ⟨110⟩ or ⟨1$\bar{1}$0⟩ direction, the g_ξ value of the C line is estimated from the data for $B \parallel \langle 110 \rangle$. These angular variations of the A, B and C lines suggest Ti^{3+} centres with spin $S = \frac{1}{2}$.

Table 2. Spin Hamiltonian parameters and polar angles of the principal axis directions of Ti^{3+} in $CaYAlO_4$. The unit of the polar angles is degrees.

Centre	Temperature (K)	g_ξ	g_η	g_ζ	θ_ξ	ϕ_ξ	θ_ζ	ϕ_ζ
A	15	1.815	1.928	1.948	180	0	90	0
B	250	1.920	1.949	1.985	170	0	80	0
C	7	1.883	—	—	90	45	—	—

5. Discussion

Ti^{3+} has the electron configuration $3d^1$. The ^2D state of $3d^1$ ions in an octahedral field splits into a $^2T_2$ ground and ^2E excited states with energy separation $10Dq$. In tetragonal symmetry, the $^2T_2$ ground state is further split into a $^2B_2$ ($|xy\rangle$) and ^2E ($|yz\rangle$, $|zx\rangle$) states. Whether the orbital doublet (^2E) or the singlet ($^2B_2$) is lower is determined by the octahedron being elongated or compressed, respectively, along the z axis. The $^2T_2$ state in orthorhombic symmetry splits into three non-degenerate orbital states. The ^2E excited state is split further into A_1 ($|2z^2-x^2-y^2\rangle$) and B_1 ($|x^2-y^2\rangle$) states by a tetragonal distortion. If the octahedron of the Ti^{3+} ion is elongated, the A_1 state is lower in energy. The lowest excited state in orthorhombic symmetry is represented by a linear combination of the A_1 and B_1 states. First we discuss the identification of Ti^{3+} in $CaYAlO_4$ according to the EPR results.

5.1. *EPR spectra*

The anisotropy of the g tensor of Ti^{3+} can deduce which of the $|xy\rangle$, $|yz\rangle$ and $|zx\rangle$ orbital states is the lowest component of the $^2T_2$ ground state of Ti^{3+} in $CaYAlO_4$. Here, the notations x, y and z correspond to the a, b and c axes of the crystal in figure 1, respectively. The EPR result that the principal ζ axis of the A line is parallel to the $\langle 100\rangle$ direction (a axis) indicates that the $^2T_2$ ground state is represented by $|yz\rangle$. Figure 9 shows energy levels of Ti^{3+} in an orthorhombic distorted octahedron, which is dominantly stretched along the c axis and additionally compressed along the a axis.

The g factor for the pure $|yz\rangle$ ground state of Ti^{3+} in orthorhombic symmetry as shown in figure 9 is calculated in terms of the spin–orbit perturbation and given by [11–14]

$$g_\xi = g_e - \frac{2\lambda}{\delta_1} + \frac{\lambda^2}{2\delta_1^2} - \frac{\lambda^2}{2\delta_2^2} + \frac{2\lambda^2}{\delta_2\Delta_2} - \frac{3\lambda^2}{2\Delta_1^2} - \frac{\lambda^2}{2\Delta_2^2} \tag{3}$$

$$g_\eta = g_e - \frac{2\lambda}{\delta_2} - \frac{\lambda^2}{2\delta_1^2} + \frac{\lambda^2}{2\delta_2^2} + \frac{3\lambda^2}{\delta_1\Delta_1} - \frac{\lambda^2}{\delta_1\Delta_2} - \frac{3\lambda^2}{2\Delta_1^2} - \frac{\lambda^2}{2\Delta_2^2} \tag{4}$$

$$g_\zeta = g_e - \frac{6\lambda}{\Delta_1} - \frac{2\lambda}{\Delta_2} - \frac{1}{2}\left(\frac{\lambda}{\delta_1} + \frac{\lambda}{\delta_2}\right)^2 + \frac{3\lambda^2}{2\Delta_1^2} + \frac{\lambda^2}{2\Delta_2^2} \tag{5}$$

where λ ($= k\zeta$) is the effective spin–orbit parameter, k is the orbital reduction factor which takes into account the covalency, ζ (=154 cm^{-1}) is the one-electron spin–orbit parameter, and δ_1, δ_2, Δ_1 and Δ_2 are the energy separations as shown in figure 9. The g shift of g_ζ from g_e (= 2.0023) is much smaller than those of g_ξ and g_η because the energies Δ_1, Δ_2 are significantly larger than the energies δ_1, δ_2.

The g values of the A line are $g_\xi = 1.815$ ($B \parallel c$), $g_\eta = 1.928$ ($B \parallel b$) and $g_\zeta = 1.948$ ($B \parallel a$) as given in table 2. The observed g values are in the order $2 > g_\zeta > g_\eta > g_\xi$. The g values derived from equations (3)–(5) show that the Ti^{3+}

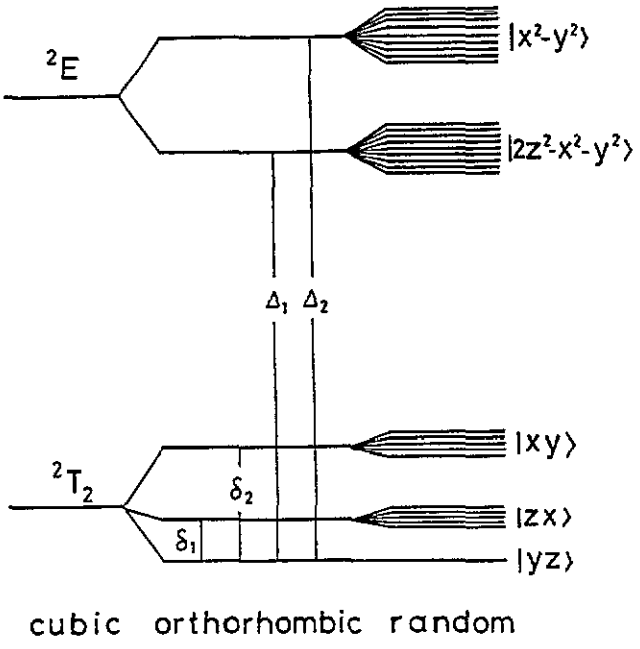

Figure 9. Energy diagram of Ti^{3+} in cubic and orthorhombic symmetries.

ground state should split into three sublevels $|yz\rangle$, $|zx\rangle$ and $|xy\rangle$ as shown in figure 9. The parameters λ/δ_1, λ/δ_2 and λ/Δ_1 in equations (3)–(5) are determined to be 0.095, 0.035 and 0.0055 by fitting the observed g values to calculated ones assuming that $\Delta_1 = \Delta_2$. The energy Δ_1 is estimated to be about 18 500 cm^{-1} assuming that the absorption band at 540 nm is due to Ti^{3+}. The effective spin–orbit parameter λ and the reduction factor k are derived to be 102 cm^{-1} and 0.66, respectively. Then, the energy separations of the ground states for the A line are $\delta_1 = 1070$ cm^{-1} and $\delta_2 = 2910$ cm^{-1}. In the same way, the parameters of the B line are estimated to be $\lambda/\delta_1 = 0.04$, $\lambda/\delta_2 = 0.025$ and $\lambda/\Delta_1 = 0.0016$.

5.2. Absorption spectra

Yamaga and co-workers [15] calculated the transition probabilities induced by odd-parity distortions, T_{1u} and T_{2u}, between the ground and excited states of Ti^{3+} in axial symmetry (tetragonal, trigonal). We apply that theory to the polarization of the absorption spectra of Ti^{3+} in $CaYAlO_4$. The T_{2u} odd-parity distortion is equivalent to the T_{1u} distortion for tetragonal symmetry. Figure 10 shows the polarization and the electric dipole transition probabilities between the $^2T_2$ ground state and the ^2E excited state induced by the z component of the T_{1u} odd-parity distortion. The transitions between the $|yz\rangle$, $|zx\rangle$ ground states and the $|x^2-y^2\rangle$, $|2z^2-x^2-y^2\rangle$ excited states are allowed, whereas those between the $|xy\rangle$ ground state and the $|x^2-y^2\rangle$, $|2z^2-x^2-y^2\rangle$ excited states are still forbidden. The electric dipole transitions are only the x and y components. This result agrees with the polarization of the absorption spectrum observed in the AS#H_2TI:CYA sample (see figure 3(a)). These optical transitions are parity-allowed transitions induced by the z component of the T_{1u} odd-parity distortion because of the large absorption coefficients, although there remains the problem of which of the bands, that with the peak at 408 nm or that with the peak at 540 nm, corresponds to Ti^{3+}.

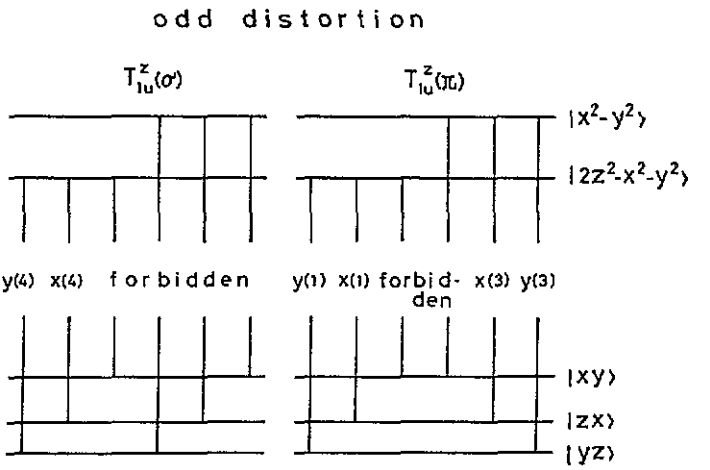

Figure 10. Polarization and relative intensities of optical transitions of Ti^{3+} induced by the z component of T_{1u} odd distortion. σ and π imply that ligand ion displacements are parallel to and perpendicular to the central ion/ligand ion axis, respectively (see figure 11).

5.3. A model of the Ti^{3+} centre

The broad absorption bands with the peaks at 408 nm and 540 nm are due to the complexes of Ti ions and O^{2-} vacancies, according to the relation of the sample preparation and the optical absorption spectra. The polarization of the absorption spectrum suggests that the Ti^{3+} octahedron is distorted along the c axis with odd symmetry. In addition, the EPR analysis deduces that the Ti^{3+} octahedron is dominantly elongated toward the c axis and additionally compressed along the a or b axis with orthorhombic symmetry. These results are, however, inconsistent with the result obtained from the analysis of the $CaYAlO_4$ crystal structure that an Al^{3+} octahedron is compressed along the c axis with tetragonal symmetry [8].

In order to remove this discrepancy, we propose a model where a Ti^{3+} octahedron is accompanied by an $O^{2-}(3)$ ligand ion vacancy on the c axis as shown in figure 11. The $O^{2-}(3)$ vacancy, acting as an effective positive charge, produces the z component of a T_{1u} odd static distortion and an expansion of the octahedron along the z (c) axis. This configuration can explain the polarization of the absorption spectrum (see figures 3(a) and 10). However, a distortion along the a or b axis other than that created by the $O^{2-}(3)$ vacancy is required in order to explain the EPR results.

We propose the following models for the origin of axial fields perpendicular to the c axis.

(1) A Ti^{4+} ion replaces the neighbouring Al^{3+} ion on the a axis in figure 12(A). The Ti^{4+} ion attracts the $O^{2-}(1)$ ligand ion slightly because of the high valency of Ti^{4+}. Then, an axial field is created along the Ti^{4+}–O^{2-}–Ti^{3+} axis.

(2) A vacancy is created at the neighbouring Al^{3+} ion site on the a axis in figure 12(B). The Al^{3+} vacancy is effectively negative charge. The combination of the Al^{3+} vacancy on the a axis and the $O^{2-}(3)$ vacancy on the c axis rotates the $O^{2-}(1)$–Ti^{3+} axis of the octahedron toward the c axis.

(3) A vacancy is created at the neighbouring Al^{3+} ion site with the $\langle 110 \rangle$ direction or a Ti^{4+} ion replaces the Al^{3+} ion in figure 12(C). This effect produces an axial field parallel to the $\langle 110 \rangle$ direction.

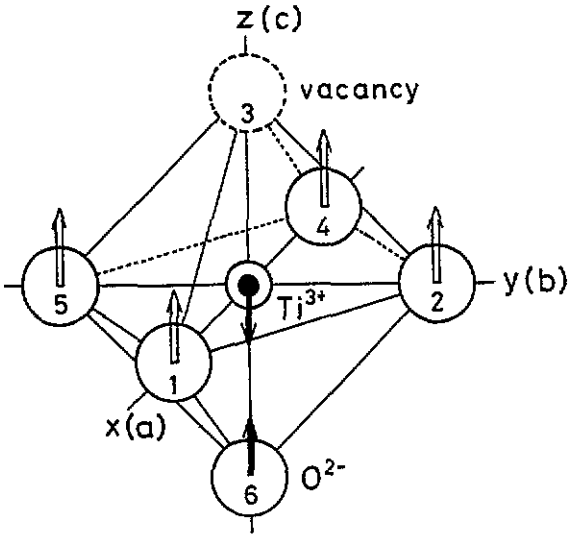

Figure 11. A proposed model for a Ti^{3+} centre. Arrows (→ and ⇒) show the z components of $T_{1u}(\sigma)$ and $T_{1u}(\pi)$ distortions, respectively.

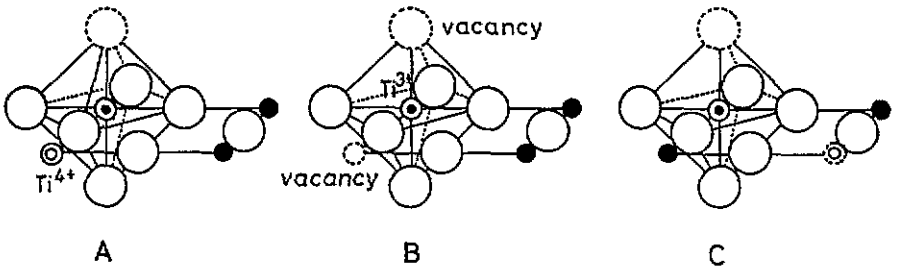

Figure 12. Ti^{3+} octahedra perturbed by an O^{2-} vacancy on the z (c) axis and by either an Al^{3+} vacancy or a Ti^{4+} ion at neighbouring Al^{3+} sites perpendicular to the z (c) axis.

Next, we consider which of the models 1–3 corresponds to the A, B and C lines. The EPR line shape and resonance field position of the A line change gradually with the increase of temperature. The g_ξ and g_η values change from 1.74 to 1.88 and from 1.89 to 1.94, respectively, as temperature increases from 4.2 K up to 90 K as shown in figure 6. The g values are given as a function of the splittings δ_1 and δ_2 in equations (3)–(5). The spreads of δ_1 and δ_2, being estimated to be $\sim$ 770–1670 cm^{-1} and $\sim$ 1800–3300 cm^{-1}, respectively, from the variations of the g values, are caused by the random distribution of Ca^{2+} and Y^{3+}ions because they have different valencies and ionic radii. The randomness produces the energy widths ($\sim$1000 cm^{-1}) of δ_1 and δ_2, as shown in figure 9. Taking account of these results, the A line is assigned to be model 1 where a Ti^{3+} octahedron is perturbed by the O^{2-}(3) vacancy and the Ti^{4+} ion on the a axis (b axis) as shown in figure 12(A).

The g_ξ, g_η and g_ζ values for the B line are 1.920, 1.948 and 1.985, respectively. The values of δ_1 and δ_2 for the B line are estimated to be 2500 cm^{-1} and 4000 cm^{-1}, respectively, from the g values. The splitting, δ_1, for the B line is about twice as large as that for the A line and also much larger than the energy width ($\sim$1000 cm^{-1}) produced by the randomness.

These results are consistent with the fact that the temperature variations of the g_ξ, g_η and g_ζ values for the B line are fairly small in the range of 4.2–250 K. In addition, the principal ζ axis of the B line is bent by 10° from that of the A line to the c axis. Then, the B line is assigned to be model 2 where a Ti^{3+} octahedron is perturbed by the $O^{2-}(3)$ vacancy and the Al^{3+} vacancy on the a axis (b axis) as shown in figure 12(B). In the same way, the C line is due to model 3 as shown in figure 12(C).

Finally we assign the two absorption bands with peaks at 408 nm and 540 nm shown in figure 3(a), the full widths at half maximum (FWHMs) of which are 1900 cm^{-1} and 2800 cm^{-1}, respectively. The FWHM of the 408 nm absorption band is nearly equal to that (1950 cm^{-1}) of the 275 nm excitation band from isolated Ti^{4+} ions as shown in figure 4. The $O^{2-}(3)$ vacancy may weaken the crystal fields of the Ti^{4+} and Ti^{3+} octahedra. In consequence, the absorption bands are expected to be shifted to lower energy. Then, the 408 nm and 540 nm absorption bands are due to the Ti^{4+} and Ti^{3+} octahedra perturbed dominantly by the $O^{2-}(3)$ vacancy, respectively.

6. Conclusions

Ti-doped $CaYAlO_4$ single crystals were grown in a reducing atmosphere. The two absorption bands with peaks at 408 nm and 540 nm were observed at room temperature. The luminescence from Ti^{4+} shows the broad band with the peak at 465 nm observed at room temperature, whereas that from Ti^{3+} could not be observed at helium and room temperatures. In order to make it clear why Ti^{3+} luminescence could not be observed in the crystal, EPR measurements were carried out in the temperature range of 4.2–300 K. The EPR results and the polarization of the absorption spectrum have shown that Ti^{3+} octahedra in the crystal are accompanied by O^{2-} ligand ion vacancies on the c axis. In consequence, local phonons created around the O^{2-} vacancy enhance the non-radiative decay rate from the ^2E excited to the $^2T_2$ ground state of Ti^{3+}.

The O^{2-} vacancies in the crystal are produced in a reducing atmosphere, which is required to convert Ti^{4+} to Ti^{3+} in the crystal. The pressure ratio of H_2 gas to inert gas (He or Ar) is a very important parameter for the crystal growth to create Ti^{3+} radiative centres in $CaYAlO_4$ crystals. Therefore, severe control of the gas ratio is required in order to prevent creation of O^{2-} vacancies in the crystal.

References

[1] Walling J C 1987 *Tunable Lasers* ed L F Mollenauer and J C White (Berlin: Springer) ch 9
[2] Moulton P 1982 *Opt. News* **8** 9
[3] Wegner T and Petermann K 1989 *Appl. Phys.* B **49** 275
[4] Petermann K 1990 *Opt. Quantum Electron.* **22** S199
[5] Sugano S, Tanabe Y and Kamimura H 1970 *Multiplets of Transition Metal Ions in Crystals* (New York: Academic)
[6] Wyckoff R W G 1964 *Crystal Structure* vol 2 (New York: Interscience) p 7
[7] Diehl R and Brandt G 1975 *Mater. Res. Bull.* **10** 85
[8] Oudalov J P, Daoudi A, Joubert J C, Flem G L and Hagenmuller P 1970 *Bull. Soc. Chim. France* **10** 3408
[9] Yamaga M, Naitoh Y and Kodama N 1993 *Proc. XII Int. Conf. on Defects in Insulating Materials* ed O Kanert and J M Spaeth (Singapore: World Scientific) p 173
[10] Yamaga M, Yosida T, Hara S, Kodama N and Henderson B 1994 *J. Appl. Phys.* **75** 1111
[11] Yamaga M, Yosida T, Henderson B, O'Donnell K P and Date M 1992 *J. Phys.: Condens. Matter* **4** 7285
[12] Abragam A and Bleaney B 1970 *Electron Paramagnetic Resonance of Transition Ions* (Oxford: Clarendon) chs 7, 10

[13] Pilbrow J R 1990 *Transition Ion Electron Paramagnetic Resonance* (Oxford: Clarendon) chs 3, 5
[14] Wertz J E and Bolton J R 1972 *Electron Spin Resonance: Elementary Theory and Practical Applications* (New York: McGraw-Hill) ch 12
[15] Yamaga M, Henderson B and O'Donnell K P 1991 *Appl. Phys.* B **52** 122